Materials & Design 253 (2025) 113861

Contents lists available at ScienceDirect

Materials & Design

journal homepage: www.elsevier.com/locate/matdes

$2H\text{-}MoS_2$ lubrication-enhanced MWCNT nanocomposite for subtle bio-motion piezoresistive detection with deep learning integration[☆]

Ke-Yu Yao [a], Derek Ka-Hei Lai [a], Hyo-Jung Lim [a], Bryan Pak-Hei So [a], Andy Chi-Ho Chan [a], Patrick Yiu-Man Yip [e], Duo Wai-Chi Wong [a,c,*], Bingyang Dai [a], Xin Zhao [f], Siu Hong Dexter Wong [d,g,*], James Chung-Wai Cheung [a,b,c,*]

[a] Department of Biomedical Engineering, Faculty of Engineering, The Hong Kong Polytechnic University, Hong Kong 999077, China
[b] Research Institute of Smart Ageing, The Hong Kong Polytechnic University, Hong Kong 999077, China
[c] Research Institute for Sports Science and Technology, The Hong Kong Polytechnic University, Hong Kong 999077, China
[d] School of Medicine and Pharmacy, Ocean University of China, Qingdao 266003, China
[e] Department of Electrical and Electronic Engineering, Faculty of Engineering, The Hong Kong Polytechnic University, Hong Kong 999077, China
[f] Department of Applied Biology and Chemical Technology, Faculty of Science, The Hong Kong Polytechnic University, Hong Kong 999077, China
[g] Laboratory for Marine Drugs and Bioproducts, Qingdao Marine Science and Technology Center, Qingdao 266237, China

ARTICLE INFO

Keywords:
Flexible piezoresistive sensor
MWCNT/MoS_2 nanocomposite
Lubrication toughening
Deep learning
Subtle-to-moderate biophysical signal

ABSTRACT

Intelligent piezoresistive health monitoring systems integrate advanced nanocomposite architectures with precise algorithmic analysis for real-time physiological assessment. However, existing works often prioritize high sensitivity at the expense of strain tolerance and require complex fabrication procedures. Herein, we present an environmentally friendly, low-cost, and nonionic fabrication approach for a 2H-phase molybdenum disulfide ($2H\text{-}MoS_2$)-enhanced multi-walled carbon nanotube (MWCNT) strain sensor, developed via a systematically optimized vacuum-assisted filtration process. This study is the first to validate the dual enhancement effect of MoS_2, leveraging its shear-exfoliation properties to simultaneously improve strain gauge performance and mechanical robustness. The resulting nacre-like layered hybrid nanocomposite achieves a remarkable gauge factor of 675.7 (R^2~0.993) at low strain (~0–4.5 %), representing a 3881.5 % improvement over pure MWCNT systems, alongside enhanced toughness (~89.17 %) and strain tolerance (~53.93 %). Meanwhile, the optimized composition ensures low rest-state resistance (~13.1 Ω), minimal hysteresis (~5.7 %), and robust durability over 5000 cycles at 10 % strain. As a result, the proposed sensor enables highly consistent, high-fidelity monitoring of various subtle-to-moderate biomotions. Integrated with a fine-tuned InceptionTime deep learning model, it achieves an F1-score of 98 % in classifying Dysphagia Diet Standardization Initiative (IDDSI)-standard swallowing activities, demonstrating its potential for AI-driven health monitoring applications.

1. Introduction

Intelligent biophysical signal monitoring, powered by advanced sensing technologies and deep learning, is critical for real-time health assessment and early abnormality detection. Subtle physiological signals, such as neuromuscular activities, provide essential insights into motor control and coordination [1–3]. Swallowing detection, for instance, plays a vital role in diagnosing and managing dysphagia—a condition associated with severe complications like aspiration pneumonia and choking-related anxiety [4]. However, conventional sensor-based approaches, including electromyography, microphones, and sonic/subsonic sensors, have demonstrated limited accuracy (<70 %) due to inherent sensor constraints, inconsistent measurement protocols, and suboptimal data analysis techniques [5–7].

Piezoresistive sensors, which convert mechanical deformation into electrical signals via percolation network evolution, are widely adopted in wearable sensing applications due to their low power consumption, facile signal acquisition, and scalability [8]. Among various structural designs, sandwiched piezoresistive architectures, in which an elastic matrix encapsulates a central sensing layer, efficiently localizes

---

[☆] This article is part of a special issue entitled: ‘AI Materials’ published in Materials & Design.

[*] Corresponding authors.

E-mail addresses: duo.wong@polyu.edu.hk (D.W.-C. Wong), dexterwong@ouc.edu.cn (S.H.D. Wong), james.chungwai.cheung@polyu.edu.hk (J.C.-W. Cheung).

https://doi.org/10.1016/j.matdes.2025.113861
Received 6 January 2025; Received in revised form 28 February 2025; Accepted 19 March 2025

mechanical stress, facilitating network disruption upon deformation and achieving high sensitivity at subtle-to-moderate strain levels. To enhance sensing performance and multifunctionality, researchers have advanced prominent sensing structures, such as micro-patterned interfaces [9,10], segregated conductive networks [11], and hierarchical hybrid systems integrating zero-dimensional (0D) to two-dimensional (2D) functional fillers [12–15]. Despite significant advancements, many of these designs require complex fabrication, precise templating, or extensive structural optimization. Moreover, densely percolated sensing networks, particularly those formed by high-aspect-ratio nanomaterials like carbon nanotube-based buckypaper, exhibit inherent mechanical rigidity (elastic modulus ~0.95 TPa), limited strain tolerance (strain-to-failure ~0.5 %), and susceptibility to interfacial delamination [16,17]. These constraints hinder resilience to intricate deformation modes, such as overextension and multidirectional strain, resulting in unpredictable electromechanical responses in practical applications. Thus, a key challenge remains in developing scalable, cost-effective nanocomposites that achieve high sensitivity, maintain a linear response at low strain, and endure larger deformations for extended usability.

Molybdenum disulfide (MoS_2), a transition metal dichalcogenide (TMD), has garnered significant interest for its distinct electronic phases, existing in metallic 1 T and semiconducting 2H configurations [18]. Its layered van der Waals structure provides exceptional mechanical flexibility, a high surface-to-volume ratio, and tunable electronic properties [14,19]. These characteristics make MoS_2 an versatile filler for piezoresistive sensors either as a standalone active material [14,20,21] or as a reinforcement in hybrid sensing architectures [19,22–25]. Beyond its electronic versatility, MoS_2 is renowned for its interfacial sliding dynamics, facilitating shear-induced exfoliation with an ultralow friction coefficient ($\sim 10^{-4}$) in its incommensurate 2H phase monolayer configuration [19,26]. This lubrication mechanism has been extensively explored in structural engineering to mitigate stress concentrations and enhance mechanical resilience through energy dissipation, akin to the “brick-and-mortar” architecture of natural nacre [27–29]. Recent studies have also preliminarily explored the lubrication role of MoS_2 in loosely packed hybrid piezoresistive networks, such as MWCNT/MoS_2 [25] and silver nanofiber (AgNF)/MoS_2 composites [23], demonstrating enhanced gauge sensitivity through nanoscale junction segregation and elastic-sliding interactions. However, these studies have primarily focused on electromechanical enhancements while neglecting their impact on mechanical reinforcement within sensing architectures. To date, the dual role of MoS_2’s interlayer sliding in a densely packed buckypaper-based sensing film has yet to be thoroughly explored and validated. This presents a compelling opportunity to achieve a “two birds with one stone” effect: improving gauge factor and overall sensing capabilities for precise strain detection while reinforcing structural integrity to withstand unexpected deformations, addressing the critical challenge in advancing sandwiched piezoresistive sensors.

Beyond sensor development, accurate classification of swallowing and other subtle biomotions is often hindered by the limitations of conventional machine learning models. These approaches struggle with the complex, time-dependent nature of physiological signals, leading to suboptimal classification accuracy [30,31]. These models typically rely on predefined features, which may not adequately capture the nuanced differences between normal and abnormal swallowing patterns. Swallowing abnormalities can stem from various factors, including physical alterations, muscle weakness, and coordination deficits, often making them difficult to identify using conventional sensors and machine learning models. Besides, deep learning has emerged as a powerful tool for time-series classification, with models such as Long Short-Term Memory (LSTM) networks, transformers, and hybrid architectures demonstrating significant advancements. LSTMs effectively capture long-term dependencies through memory cells and gating mechanisms, making them well-suited for sequential data analysis [32]. Meanwhile, transformers, initially developed for natural language processing, leverage self-attention mechanisms to dynamically prioritize relevant temporal features, enhancing performance in time-series tasks [33]. However, these models often require extensive datasets for optimal training [34], which poses challenges in clinical applications where data collection is often constrained. Moreover, deep learning models must be fine-tuned to specific sensor inputs to achieve optimal accuracy, particularly for small datasets [35].

Among various deep learning architectures, the InceptionTime model has proven highly effective for swallowing detection and other fine-scale motion classification due to its ability to capture multi-scale temporal features [36]. Its inception module structure enables simultaneous feature extraction across multiple time scales, making it particularly well-suited for analyzing complex swallowing signal dynamics. Research has shown that InceptionTime achieves state-of-the-art classification accuracy while maintaining high computational efficiency [36]. Its adaptability to varying input sequence lengths further enhances its suitability for continuous, real-time swallowing monitoring.

In this study, we developed a 2H-MoS_2 lubricate-enhanced MWCNT strain sensor, termed MolyMWCNT-BP, using an environmentally friendly, low-cost, and nonionic fabrication approach. Through comprehensive suspension optimization and vacuum-assisted filtration refinement, we optimized the hybrid network structure. Leveraging the shear-exfoliation lubrication effect of MoS_2, the sensor exhibits enhanced gauge sensitivity and linearity in the low-strain region, enabling high-fidelity detection of various subtle-to-moderate biophysical signals. Additionally, MoS_2 integration significantly improves fracture strain, toughness, and microstructural wear resistance, while maintaining low rest-state resistance, minimal hysteresis, and robust durability. To further enhance application potential, we implemented the InceptionTime deep learning model, optimizing its architecture and hyperparameters for accurate classification of swallowing and non-swallowing tasks. This work establishes a scalable, intelligent health monitoring platform, integrating materials science and algorithmic advancements for real-time, precise physiological motion assessment.

2. Material and methods

2.1. Preparation of MWCNT-/MolyMWCNT-BPs

Detailed information on materials, including specifications and sources, has been provided in Supplementary Table S1. In brief, MWCNTs (20, 50, 100, 150, and 200 mg) were dispersed in various solvents (DI water, ethanol, or IPA) at a fixed concentration of 0.025 % w/v, with Triton X-100 added at 0.5 % v/v relative to the solvent volume. To prepare the hybrid suspension, MoS_2 powders (5, 10, 15, 20, and 25 mg) with lateral sizes of 30, 50, 80, 100, 150, and 500 nm were incorporated into the MWCNT dispersion. The suspension was magnetically stirred at 600 rpm for 30 min (MS-01DUA, Crystal Tech Co. Ltd., Suzhou, China) to ensure uniform wetting of the fillers, followed by a probe sonication step for 60 min (300 W, 50 kHz, SM-1000C, ShunmaTech Co. Ltd., Nanjing, China). A subsequent ice-bath sonication for 60 min in a sonication bath (450 W, 40 kHz, GL0810, Granbosonic Tech. Ltd., Shenzhen, China) was applied to achieve homogeneous dispersion. Post-sonication, the suspensions were centrifuged at 3000 rpm for 10 min (OK5A, Okay Energy Equipment Co., Ltd., Changsha, China), and the resulting supernatant (~0.5 mg/mL) was collected for storage and subsequent filtration.

Vacuum filtration was conducted using different hydrophilic filter membranes (MCE, nylon, and PTFE) under varying vacuum pressures levels (−0.9 MPa and −0.45 MPa). The duration was fixed at 3 h to minimize residual solvent retention within the membrane. The deposited films were carefully detached by spraying isopropyl alcohol (IPA) onto the membrane’s backside, followed by thorough rinsing with ethanol and DI water to remove any residual surfactants and impurities. The films were then dried overnight at 40 °C under uniform light pressure and subsequently baked at 70 °C for 2 h to enhance structural integrity. The optimized deposition density and deposition rate were determined as 3.5 × 10^{-3} g/cm^2 and 92.81 wt%, respectively. The experimental parameters and optimization procedures are compiled and investigated in Supplementary Table S1 and Note 1.

2.2. Fabrication of MWCNT/MolyMWCNT-BP strain sensors

The prepared MolyMWCNT-BP films were cut into sensing strips (30 mm × 5 mm) using a custom cutter. Copper foil electrodes were attached to both ends using silver paste, ensuring a thin, uniform layer for optimal adhesion. A PDMS-cured encapsulation layer was prepared by thoroughly mixing PDMS and a curing agent in a 10:1 wt ratio and coating it onto a flat glass substrate using a Mayer rod (300 μm, BuschmanTM, Cleveland, USA) for uniform thickness. The coated substrate was then subjected to vacuum degassing for 30 min, followed by soft baking at 60 °C for 45 min. For sensor assembly, one side of the MolyMWCNT-BP strip was covered with polyimide (PI) tape, while the exposed side was placed onto the semi-cured PDMS layer on the glass substrate. To achieve a compact and secure skin-side encapsulation, hot pressing at

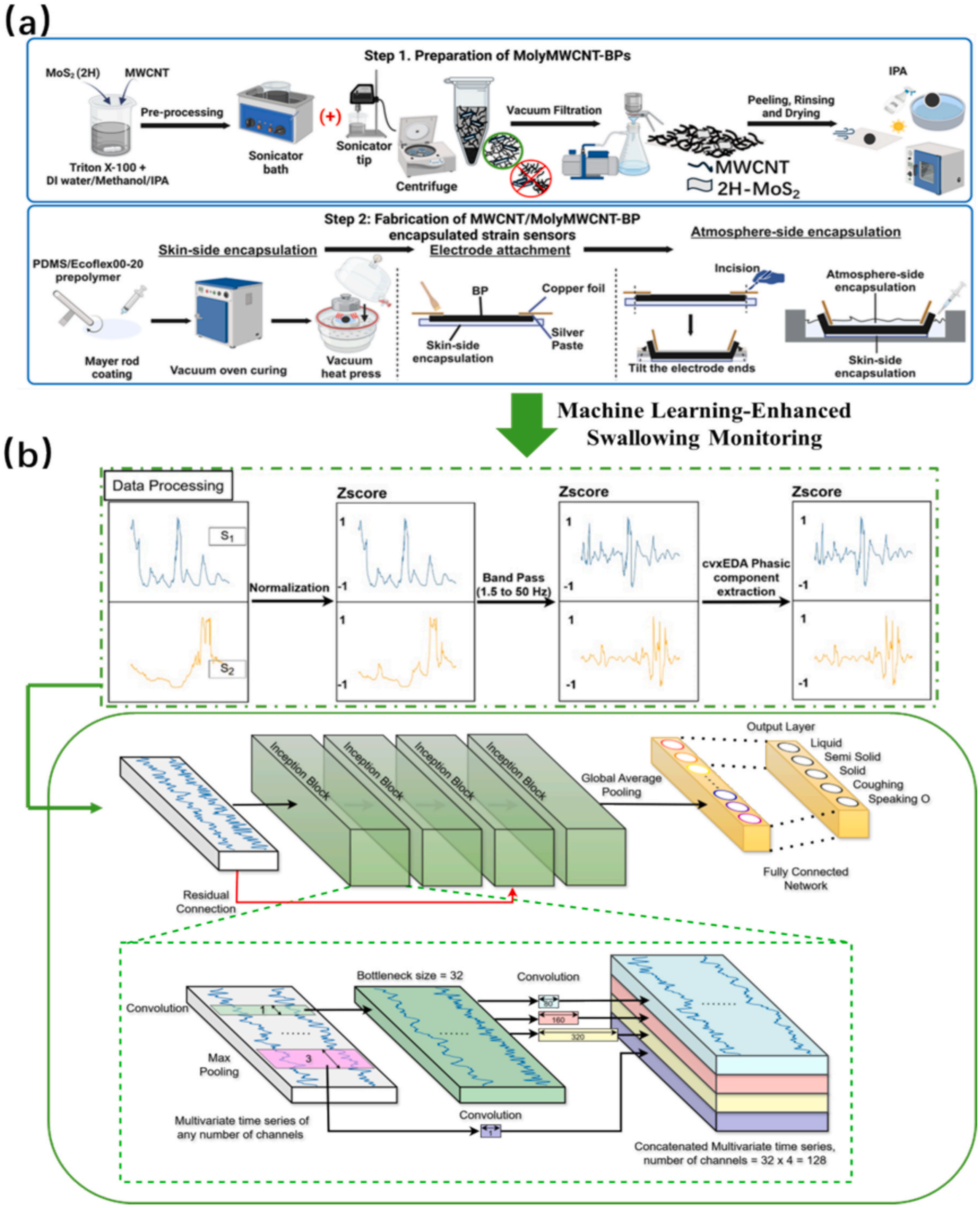

Fig. 1. Overview of sensor fabrication and, physiological signal acquisition and processing for swallowing detection. (a) MolyMWCNT-BP fabrication and encapsulation preparation procedures; (b) Data processing framework, including normalization, bandpass filtering, and cvxEDA feature extraction before classification using the InceptionTime model. The bivariate data represent the relative resistance change ($\Delta R/R_0$) collected using the paired sensor channels (S1 and S2).

100 °C for 60 min was applied. The electrode ends were elevated and fixed before transferring the encapsulated strips into a 3D-printed acrylonitrile butadiene styrene (ABS) mold (3D printer: Bamboo Lab X1, Bambu Lab, Shenzhen, China). A second encapsulation was performed by molding uncured PDMS onto the exposed surface. Additionally, an Ecoflex-encapsulated strain sensor was fabricated following the same procedure, replacing the PDMS encapsulation with Ecoflex™ 00–20 Fast. All finalized sensor samples were fabricated in accordance with ASTM D412 standards, ensuring consistency and reliability for subsequent electromechanical testing. The overall fabrication process is schematically illustrated in Fig. 1**(a)**.

2.3. Material and electromechanical characterization

An electronic analytical balance (XS105 Dual Range, Mettler Toledo, Columbus, United States) was used to precisely measure the deposited material weight in the sensing films. The surface micro-topography and microstructural features of the sensing films were analyzed using Visible Light Microscopy (VLM) (KERN OBF-1, KERN & Sohn GmbH, Balingen, Germany) and Scanning Electron Microscopy (SEM) (MIRA, Tescan Orsay Holding a.s., Brno, Czech Republic). The composition and quality of the hybrid sensing film and as-prepared strain sensor were examined by the Renishaw Micro-Raman Spectroscopy System, X-ray Photoelectron Spectroscopy (XPS) (Nexsa, Thermo Fisher Scientific Inc., Waltham, United States), X-ray Diffraction / Energy Dispersive X-ray Spectroscopy (XRD/EDS) (SmartLab 9 kW-Advance, Rigaku Corp., Tokyo, Japan), and Thermogravimetric Analysis/Differential Scanning Calorimetry (TGA/DSC) (TGA/DSC3+, Mettler Toledo GmbH, Greifensee, Switzerland) with pure N_2 gas flow. The electromechanical performance of the sensors was evaluated using a digital multimeter (RSDM3055, RS Components Limited, Corby, United Kingdom) with a 0.2 % strain interval to ensure precise resistance measurements. Samples were subjected to controlled deformation using a universal testing machine (68TM-10, Instron, Norwood, United States) equipped with a 5 kN load cell. Strain values were directly recorded using an extensometer, mitigating discrepancies from machine displacement readings. Prior to cyclic testing and application, the sensors were pre-stretched 20 cycles at 10 % strain to ensure experimental consistency. The calculation of sensing sensitivity, represented by the gauge factor (GF), and sensing hysteresis is detailed in Equations S1 and S2.

2.4. Physiological signal detection and model fine tuning

To evaluate the applicability of the MolyMWCNT-BP sensor in capturing subtle-to-moderate muscle activities, we conducted real-time physiological signal detection experiments. Five distinct actions—-blinking, frowning, wrist flexion, gripping during forearm supination, and ankle dorsiflexion—were monitored under the guidance of a professional physiotherapist. Sensors were attached to the targeted muscles using Skin Tite™ bio-adhesive, ensuring stable contact and minimal motion artifacts. The signal waveforms and frequencies were analyzed to verify their correlation with the respective physiological activities.

To further validate the sensor's capability, we extended our study to complex physiological tasks, particularly swallowing and non-swallowing activities. Two MolyMWCNT-BP sensors were placed on each participant's neck, positioned at the hyoid bone and 5 cm below it, to capture biomechanical signals associated with swallowing. To ensure accurate signal acquisition, all subjects performed swallowing, coughing, and speaking tasks in synchronization with predefined prompts. Given the dynamic nature of neck movements, including rotational and postural variations [37], we standardized the testing conditions by instructing participants to maintain a stable sitting posture in a controlled, low-noise environment to minimize external disturbances. The detailed swallowing experiment procedures are detailed in Supplementary Note 3.

The sensor data collected during swallowing and non-swallowing tasks were split into training and testing sets (80:20 ratio). To improve model robustness, we applied data augmentation techniques, including jittering, time warping, and window warping. A comprehensive data preprocessing pipeline (Fig. 1**(b)**) was implemented. The process began with Z-score normalization, followed by timestamp alignment, which ensured precise segmentation by extracting only the signals corresponding to the intended action while filtering out motion artifacts. Next, bandpass filtering (1.5 to 50 Hz) was applied to isolate relevant frequency components and minimize noise from unintended strain variations (such as heartbeat and breathing) and electrical noise, respectively. Additionally, cvxEDA, with default parameter settings, was utilized to extract physiological responses specifically related to swallowing [38].

We employed the InceptionTime model, a state-of-the-art time-series classifier, which features six inception modules optimized for extracting multi-scale temporal patterns via 1D convolutions of varying kernel sizes [36]. The model architecture incorporates batch normalization to stabilize learning, ReLU activation to introduce non-linearity, residual connections to mitigate gradient vanishing, and Global Average Pooling layers to reduce each feature map to a single summary value. A fully connected layer serves as the final classifier, outputting class labels for swallowing (liquid, semiliquid, solid) and non-swallowing (coughing, speaking "O") tasks. The optimization process of the InceptionTime model, including kernel size scaling, block adjustments, and performance validation, is also detailed in Supplementary Note 3.

3. Results and discussion

3.1. Material characterization

In this study, we developed a MWCNT/MoS_2 hybrid buckypaper, termed MolyMWCNT-BP, strain sensor via a scalable vacuum-assisted filtration method, leveraging MoS_2's lubrication effect to enhance gauge performance and mechanical robustness for detecting subtle-to-moderate biophysical signals (Fig. 2**(a)**). MWCNT-BP sensors without MoS_2 incorporation were fabricated as references. The nanostructures of MWCNTs and MoS_2 nanosheets were confirmed to match supplier specifications (Fig. S2(a, b)). Extensive optimization, including suspension stability refinement and vacuum filtration parameter adjustments, was conducted, as detailed in Supplementary Notes 1.

Unlike previous studies that predominantly utilized NMP (N-Methyl-2-pyrrolidone), or DMF (Dimethylformamide) as solvent for MWCNT/MoS_2 hybrid suspensions, or relied on chemical modification methods, such as in-situ hydrothermal growth or layer-by-layer self-assembly [24,25,39,40], this work employed an environmentally friendly, nonionic and cost-effective IPA/Triton X-100 system to achieve a stable MWCNT/MoS_2 suspension. Triton X-100 stabilized dispersion through amphiphilic interactions, while π-π stacking and steric hindrance prevented MoS_2 restacking, ensuring a uniform hybrid network for vacuum filtration, as schematically illustrated in Fig. 2**(b)**. The resulting composite films exhibited a well-integrated hybrid sensing network, as demonstrated by their uniform morphology and freestanding form (Fig. 2**(b) inset**). Besides, the bottom row highlights the sensor's flexibility and structural integrity, showcasing its ability to bend with a small radius.

With an overall thickness of 875 ± 31 μm, the MolyMWCNT-BP sensor demonstrated high compliance for on-skin applications. SEM analysis confirmed a well-interpenetrated MWCNT/MoS_2 network (Fig. 2**(c)**), with a nacre-like layered structure formed through the orderly cake accumulation process during vacuum filtration. The cross-sectional view revealed isotropically interconnected MWCNTs, while the limited presence of MoS_2 nanosheets suggested their preferential alignment parallel to the deposition plane [27]. Meanwhile, the sensing film (91.75 ± 3.18 μm) and PDMS encapsulation (305.23 ± 34.85 μm) exhibited minimal thickness variation, reducing structural inconsistencies and interfacial detachment risks. (Fig. S4(d, e)). The EDS

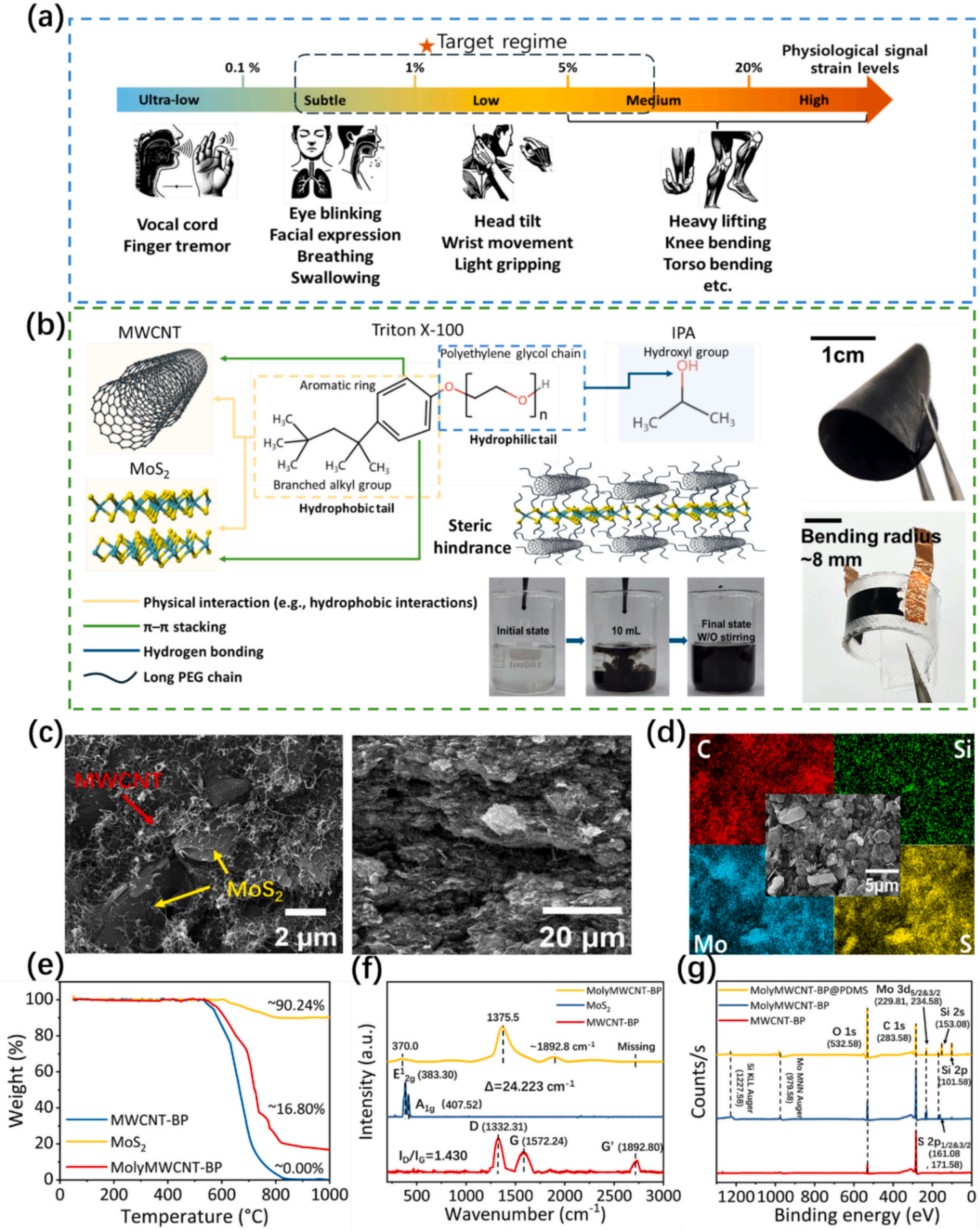

Fig. 2. Preparation and material characterization of the MolyMWCNT-BP strain sensor. (a) Schematic of biophysical signal categorization by strain levels, highlighting the sensor's target application region; (b) Hybrid suspension stabilization mechanism using the IPA/Triton X-100 system. The inset (bottom) shows a dipping test of the optimized suspension (10 mL, 0.5 mg/mL) demonstrating excellent dispersibility. Right insets display the MolyMWCNT-BP film and the encapsulated strain sensor; (c) SEM images of surface morphology and cross-sectional structure of the MWCNT-BP film; (d) EDS elemental mapping of the MWCNT-BP film; (e-f) TGA and Raman spectra of MWCNT-BP, 2H-MoS_2 (50 nm), and MolyMWCNT-BP.; (g) XPS spectra of MWCNT-BP, MolyMWCNT-BP, and the PDMS-encapsulated strain sensor.

elemental mapping confirmed a well-distributed hybrid network in the MolyMWCNT-BP sample, with carbon (C), molybdenum (Mo), and sulfur (S) corresponding to MWCNTs and MoS_2, respectively (Fig. 2**(d)**). The normalized elemental concentrations in wt% aligned well with the coating ratio in the vacuum filtration suspension, indicating high fabrication repeatability and experimental precision (Fig. S4(f)).

To ensure compositional integrity and performance consistency, TGA, Raman, and XPS analyses were conducted, as the dual-phase (metallic/semiconducting) nature of MoS_2 and residual surfactants could influence electromechanical properties. TGA results showed significant weight loss (~90–95 wt%) in MWCNT-BP between 531 °C and 826 °C, attributed to MWCNT decomposition [41], whereas MoS_2 remained thermally stable with minor weight loss above 604 °C, accounting for ~9.76 wt% of the sample (Fig. 2**(e)**). The MolyMWCNT-BP sample, optimized with 10 mg MoS_2 and 50 mg MWCNTs, exhibited a two-stage decomposition process: ~79.21 % weight loss between 544 °C and 826 °C from MWCNT decomposition, leaving a stable residue of ~16.8 wt% corresponding to MoS_2, confirming the expected composition. Raman spectroscopy in Fig. 2**(f)** further validated the presence of both MWCNTs and MoS_2, with characteristic D, G, and G' bands at ~1332.31, 1572.24, and 1892.80 cm^{-1}, respectively. The in-plane E^1_{2g} and out-of-plane A_{1g} vibration modes of MoS_2 appeared at ~383.30 cm^{-1} and 405.52 cm^{-1}, respectively [23,42]. Notably, the $I_{E^1_{2g}}/I_{A_{1g}}$ intensity ratio of ~1.37 indicated a few-layer MoS_2 structure, confirming effective dispersion achieved through optimized preprocessing. Additionally, the peak separation of ~22.22 cm^{-1} verified the retention of the 2H phase with minimal sulfur vacancies [14]. The I_D/I_G ratio of MWCNTs, measured at 1.430, indicated structural defects likely caused by oxidation or thermal degradation during processing [42]. Lastly, XPS analysis in Fig. 2**(g)** confirmed MoS_2 integration within the

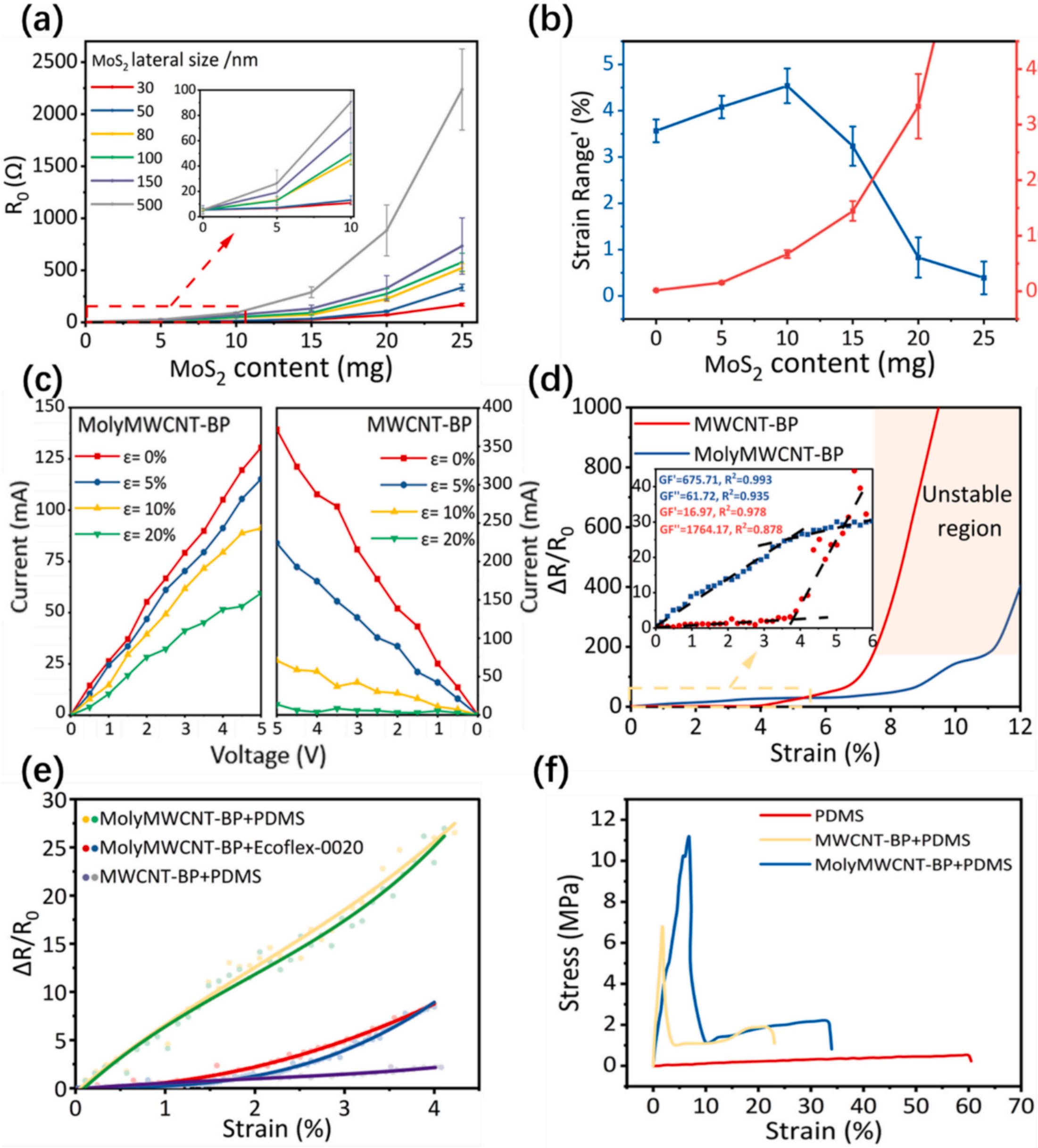

Fig. 3. Electromechanical performance comparison of MWCNT-BP and MolyMWCNT-BP strain sensors. (a) Rest-state electrical resistance (R_0) with varying MoS_2 parameters. Inset: magnified region at low MoS_2 content; (b) Strain range and gauge factor variations in the first linear sensing region (as indicated by superscript) for different MoS_2 contents (50 nm nanosheet size); (c) I-V response curves at varying strain levels; (d) Relative resistance change ($\Delta R/R_0$) before strain-to-electrical breakdown. Inset: detailed view of the first linear working range; (e) $\Delta R/R_0$ over a full stretching-releasing cycle at 4 % strain, comprising PDMS and Ecoflex™ 00 20 Fast encapsulation; (f) Tensile stress–strain curves of pure PDMS and sensors made from MWCNT-BP and MolyMWCNT-BP.

MolyMWCNT-BP composite, with distinct Mo 3d and S 2p peaks (229.81–234.58 eV and 161.08–171.58 eV, respectively) observed in the MolyMWCNT-BP spectrum but absent in MWCNT-BP alone [42,43]. Additionally, Si 2 s and Si 2p peaks confirmed strong adhesion between PDMS and the MolyMWCNT-BP sensing layer. Collectively, these results validate the formation of a high-quality, well-integrated hybrid strain sensor with a physically stacked, highly uniform network, ensuring consistent electromechanical performance, as explored in the following sections.

3.2. Composition optimization for lubrication enhancement

To elucidate the exfoliation lubrication effect of MoS_2 within the hybrid hierarchical structure and its ramifications on electromechanical performance, comprehensive mechanical and electrical characterizations were conducted. The MWCNT content was standardized across all samples to ensure consistent film quality and high reproducibility, as delineated in Supplementary Note 2.

The MWCNT network served as a robust percolative conductive matrix, while the integration of MoS_2 nanosheets introduced notable variations in the rest-state resistance (R_0) of MolyMWCNT-BP samples, as depicted in Fig. 3**(a).** Resistance increased with higher MoS_2 content across all nanosheet sizes, with larger nanosheets exerting a more pronounced effect. This trend was primarily attributed to the semiconducting 2H phase of MoS_2, which introduced localized high-resistance regions within the conductive network [19]. In samples containing smaller nanosheets (30–80 nm) and lower MoS_2 concentrations, the MWCNT network remained largely intact (Fig. S2(c)), preserving efficient electron transport pathways. However, at higher MoS_2 concentrations, the conductive network became increasingly fragmented by larger, well-defined MoS_2 flakes, which acted as resistive barriers, significantly increasing overall resistance. Maintaining low baseline resistance in piezoresistive strain sensors is crucial for minimizing power consumption, thereby improving their potential for miniaturized, integrated, and durable wearable monitoring systems.

Ensuring high sensitivity and an extended strain range within the initial linear region, as indicated by Gauge Factor' and Strain Range', of the relative resistance change-strain response is crucial for accurately capturing subtle-to-moderate biophysical signals, enabling precise data acquisition and simplifying algorithmic processing. both indicators exhibit strong correlations with MoS_2 content and nanosheet size in MolyMWCNT-BP sensors. Overall, the Gauge Factor' increased with MoS_2 content across all nanosheet sizes; however, a significant rise in signal volatility among the three as-prepared samples, reflected by larger standard deviations, indicated reduced sensor reliability at higher concentrations. A more distinct trend was observed in the Strain Range', where for MoS_2 nanosheets below 100 nm, moderate incorporation extended the linear range, while excessive content disrupted it. In contrast, for lateral sizes over 100 nm, a net destroy in strain range was observed. These findings highlight the modified microstructural evolution induced by MoS_2 incorporation and emphasize the need to optimize nanosheet size and content to effectively leverage its lubrication-enhancement effect while maintaining sensor reliability.

Notably, incorporating 10 mg of 50 nm MoS_2 nanosheets extended the Strain Range' by over 27.3 %, concurrently improved the Gauge Factor' by 529.4 % compared to the MWCNT-BP sample (Fig. 3**(b)**), while maintaining low rest-state resistance and high fabrication repeatability. Based on these findings, we further investigated the key sensing performance metrics of this optimized sample. As shown in Fig. 3**(c)**, both MWCNT/MolyMWCNT-BP samples exhibited highly linear Ohmic I-V responses in their rest states, confirming a well-percolated MWCNT network [23]. The voltage sweep method was employed to evaluate electrical conduction behavior, ensuring that the appropriate amount of semiconducting MoS_2 did not introduce a threshold voltage effect or disrupt the percolation-based conduction mechanism [44]. Under continuous stretching, the I-V curves of both sensors gradually flattened, indicating increased resistance. However, the MWCNT-BP sensor showed a more pronounced response, with large crack formation leading to a sharp increase in resistance, ultimately reaching 28.78 kΩ and transitioning to an insulating state. In contrast, the MolyMWCNT-BP sensor, despite an increase in resistance, maintained its piezoresistive response up to a longer strain, demonstrating improved strain tolerance.

The relative resistance changes ($\Delta R/R_0$) of the MWCNT-BP and MolyMWCNT-BP sensors prior to the electrical breakdown strain (ε) are presented in Fig. 3**(d)**, fitted by distinct piecewise linear relationship. The MolyMWCNT-BP sensor exhibited an outstanding initial linear sensing range from 0 % to 4.5 % strain, achieving a primary GF (GF') of ~ 675.71 with an R^2 of 0.993—representing a 3881.5 % improvement over the MWCNT-BP sample. Beyond 4.5 % strain, the MolyMWCNT-BP transitioned into a second stable linear regime (GF'' ~ 61.72, R2 ~ 0.935), extending the strain range up to 11.53 %. Subsequently, a sharp increase in sensitivity indicated the onset of an unstable sensing region, attributed to conductor-to-insulator electrical breakdown. In contrast, the MWCNT-BP sensor demonstrated a gradual resistance increase (GF ~ 16.97, R^2 ~ 0.978) and failed electrically at around 3.9 % strain, as evidenced by its catastrophic resistance increase. This comparison underscores a simultaneous enhancement in strain tolerance and gauge sensitivity at short strain-level of the MolyMWCNT-BP sensor.

The sensing hysteresis of both sensors during a full stretching and releasing cycle within approximately 4.0 % strain—where both samples remained within their stable working regions—is presented in Fig. 3**(e)**. Notably, the MolyMWCNT-BP sensor exhibited significantly lower hysteresis (~5.70 %) compared to the MWCNT-BP (~15.23 %), aligning closely with the ~ 2.75 % reported for a MoS_2-decorated graphene sensor in previous studies [19]. This reduction in hysteresis suggests that the flake-like MoS_2 nanosheets facilitate efficient alignment within the hierarchical network, acting as lubricating phases that enable structural rearrangements during cyclic loading. This mechanism helps maintain a stable and linear strain response, thereby enhancing sensor reliability. Additionally, the improved hysteresis stability and sensing sensitivity in the low-strain detection range were influenced by the choice of encapsulation material. As shown in Fig. 3**(e)**, the MolyMWCNT-BP sensor encapsulated with Ecoflex^{TM} 00–20 Fast exhibited significantly higher hysteresis (~25.70 %) and reduced sensitivity. This can be attributed to the material's pronounced viscoelasticity and lower elastic modulus compared to PDMS, leading to delayed recovery after deformation and inefficient stress transfer to the sensing layer. Consequently, these factors compromised the sensor's overall electromechanical performance [45].

The mechanical performance of pure PDMS and sensor samples composed of MWCNT-BP and MolyMWCNT-BP were evaluated, as shown in Fig. 3**(f)**. Both sensor samples initially exhibited a sharp increase in tensile stress, reflecting the higher stiffness of the buckypaper layers compared to the ductile PDMS matrix. This stiffness arises from the densely packed and entangled MWCNT network, forming a compact percolation structure and a self-supporting sensing film. However, the rigidity also contributed to premature failure due to localized stress accumulation, evidenced by an abrupt stress drop upon crack propagation within the sensing layers. Beyond this point, stress was primarily borne by the PDMS matrix, with partial redistribution along the fragmented buckypaper layers, leading to steeper slopes in the stress–strain curves. Notably, the MolyMWCNT-BP sensor demonstrated superior mechanical properties, with a 53.93 % increase in premature strain (6.85 % ± 0.36 %) and a 52.63 % enhancement in fracture strength (9.60 MPa ± 1.05 MPa) compared to the MWCNT-BP sensor (4.45 % ± 0.42 % and 6.29 MPa ± 1.12 MPa, respectively). These improvements align with the observed differences in strain-to-electrical breakdown behavior. Furthermore, fracture toughness was significantly enhanced by 89.17 %, increasing from 38.51 MJ/m^3 ± 3.48 MJ/m^3 to 72.85 MJ/m^3 ± 7.49 MJ/m^3, comparable to previous studies reporting improvements of approximately 102.3 % and 100 %, respectively [27,28].

To assess the sensor's practicality for stable and continuous monitoring, we assessed its dynamic response under repeated cycling at varying strain levels and stretching speeds. Fig. 4**(a)** presents the sensor's response across a strain range of 1–15 %, demonstrating instant response even at minimal strain levels. The peak resistance values exhibit strong repeatability with minor standard deviations, ensuring reliable operation up to approximately 10 % strain (8.18 ± 0.96, 16.25 ± 2.21, 32.20 ± 4.01, respectively). Beyond this threshold, increased signal fluctuations emerged, likely due to defect-induced nonlinearity. Meanwhile, the sensor's performance at a 10 % strain across different stretching speeds (25, 50, 75, 150 and 300 mm/min) is depicted in Fig. 4 **(b)**. The resistance response remained stable up to 150 mm/min, exhibiting minimal signal overshooting compared to previous MoS_2-

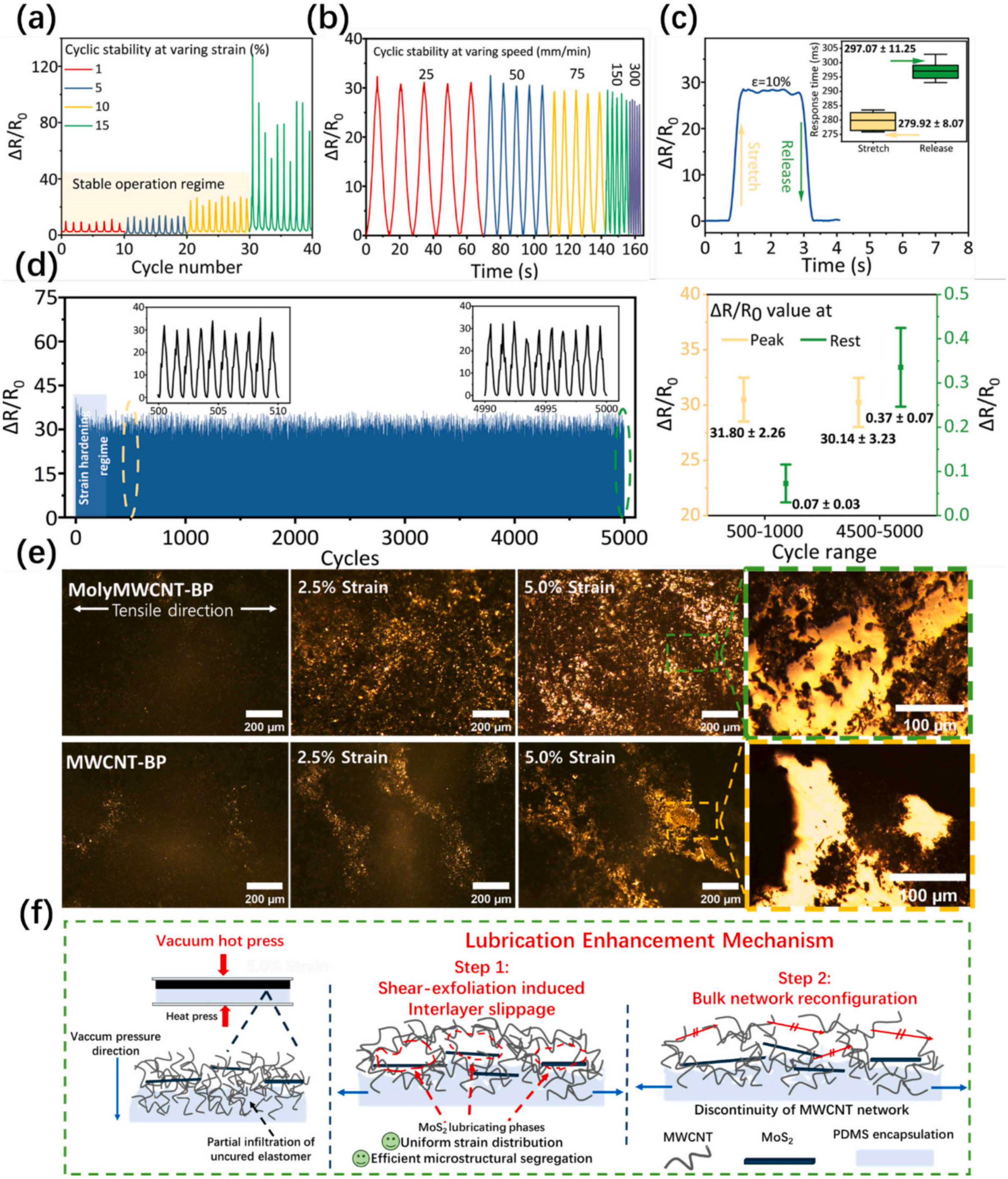

Fig. 4. Dynamic sensing performance and lubrication-enhanced mechanism of the MolyMWCNT-BP sensor. (a) Relative resistance changes across different strain levels, with the stable operating range highlighted in yellow; (b) Resistance response at ε = 10 % under various strain speeds; (c) Real-time response to a transient cycle (ε = 10 %, v = 300 mm/min). Inset: box plot showing the averaged response times over 10 cycles, with error bars representing standard deviation; (d) Fatigue resistance assessment over 5000 cycles (ε = 10 %, v = 300 mm/min). Inset comparing the averaged resistance response over 500 cycles at two different intervals for peak (yellow) and rest-state (green) phases with standard deviations; (e) Optical micrographs showing microstructural evolution of MolyMWCNT-BP and MWCNT-BP sensors within 5 % strain. Inset: magnified view of microcracks; (f) Schematic illustration of vacuum hot pressing and lubrication enhancement mechanisms. (For interpretation of the references to colour in this figure legend, the reader is referred to the web version of this article.)

based sensors [46,47]. At higher speeds, more noticeable signal fluctuations and drift emerge. This might be attributed to a combination of mechanical vibrations, dynamic strain localization, and system-induced artifacts near the upper speed limit of the tensile testing machine. Importantly, no baseline correction or signal smoothing was applied, ensuring the raw response was accurately represented. Despite these variations, the overall resistance trend remained stable, confirming the sensor's capability for dynamic strain sensing across a broad frequency range. Besides, response time tests at 10 % strain and a tensile speed of 300 mm/min, shown in Fig. 4**(c)**, yielded net response times of 219.92 ± 8.07 ms (stretching) and 237.07 ± 11.25 ms (releasing) after eliminating mechanical execution delays (~60 ms). The results, averaged over 10 continuous cycles, are now presented as a box plot in the inset, confirm consistency and suitability for physiological signal monitoring.

In the last, the fatigue performance assessed over 5000 cycles at 10 % strain (Fig. 4**(d)**). Following an initial strain-hardening phase, the sensor maintained stable operation with consistent peak resistance values. Quantitative analysis in the inset shows a slight decrease in peak resistance from 31.80 ± 2.26 to 30.14 ± 3.23, while rest-state resistance increased from 0.07 ± 0.03 (cycles 500–1000) to 0.37 ± 0.07 (cycles 4500–5000). Although visually noticeable, this shift aligns with typical

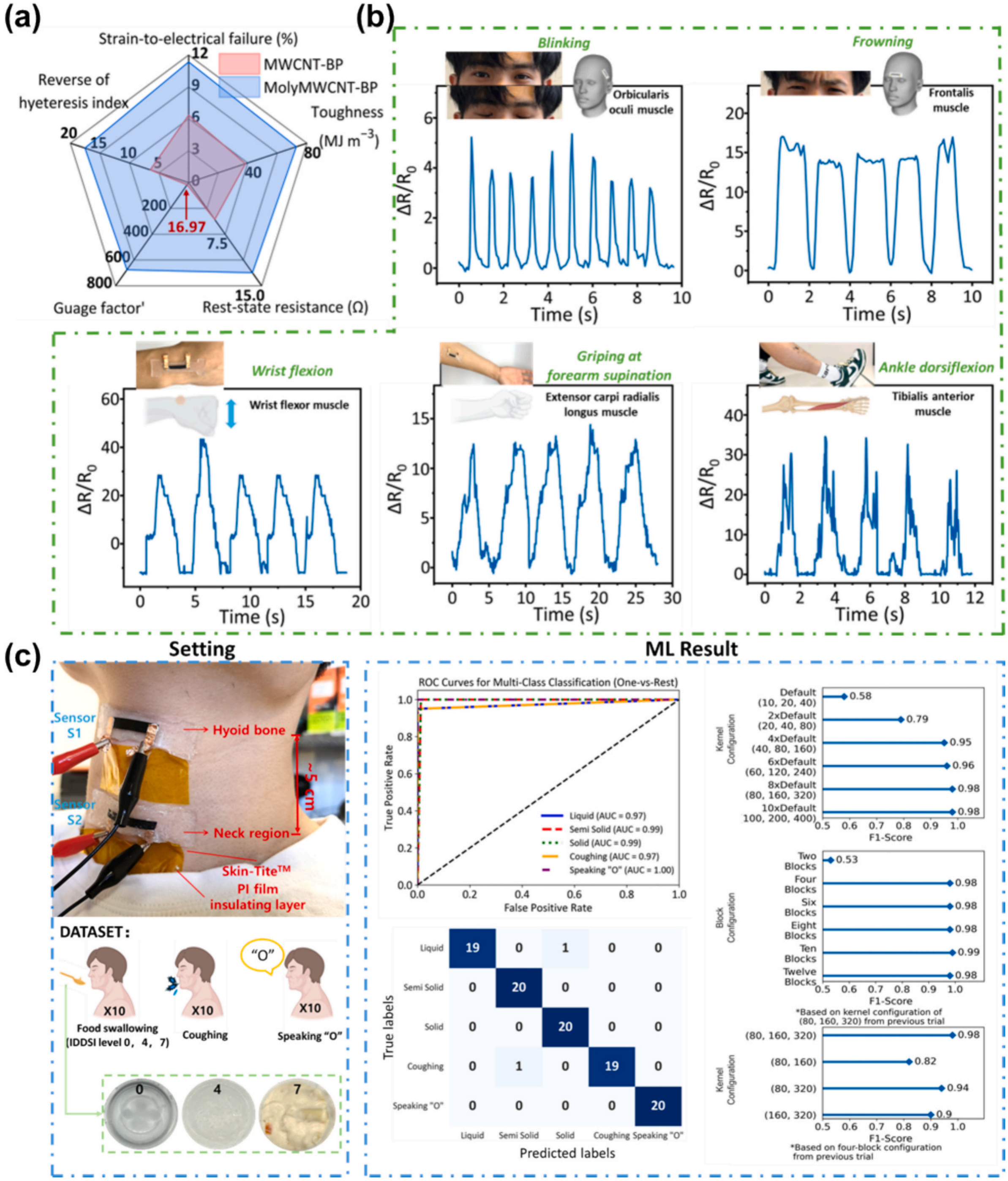

True \ Predicted	Liquid	Semi Solid	Solid	Coughing	Speaking "O"
Liquid	19	0	1	0	0
Semi Solid	0	20	0	0	0
Solid	0	0	20	0	0
Coughing	0	1	0	19	0
Speaking "O"	0	0	0	0	20

Fig. 5. Application of the MolyMWCNT-BP sensor in physiological signal detection. (a) All-aspect performance comparison between MWCNT-BP and MolyMWCNT-BP strain sensors; (b) Real time response to five subtle-to-medium amplitude muscle actions. Inset demonstrating the motion type and muscle being attached on; (c) Demonstration of the sensor placement, along with confusion matrix that illustrate the classification performance of the InceptionTime model.

fatigue effects in stretchable conductors and remains within an acceptable range. The gradual baseline drift, common in long-term cyclic loading, is attributed to microstructural rearrangement, residual strain accumulation, and interfacial contact variations. Importantly, no abrupt failure was observed, and the overall stability surpasses that of many sensors with related structure or composition reported in the literature, as comparative analyzed in Supplementary Table S2.

3.3. Lubrication enhancement mechanism analysis

To elucidate the dual role of MoS_2 in enhancing both sensing performance and mechanical robustness, the microstructural evolution of MolyMWCNT-BP under tensile strain was analyzed using optical microscopy in transmission mode, as shown in Fig. 4**(e)**. At ~ 2.5 % strain, the MoS_2-enhanced composite exhibited evenly distributed microcracks, attributed to MoS_2's layered structure promoting interfacial sliding and stress delocalization [20,25,27]. This controlled microcrack formation ensures predictable disruptions in the conductive network, enhancing strain sensitivity. As strain increased to 5.0 %, these microcracks propagated and interconnected, forming a network of defects. In contrast, MWCNT-BP displayed localized stress concentrations, with cracks propagating perpendicularly to the tensile force, leading to premature structural failure and loss of sensing capability. Future investigations utilizing in-situ SEM [26] integrated with a mechanical testing stage and atomic force microscopy could provide detailed insights into the real-time evolution of hybrid networks and the specific role of MoS_2 in piezoresistive sensing.

The exfoliation-lubrication and toughening mechanisms of MoS_2 in MolyMWCNT-BP are schematically illustrated in Fig. 4**(f)**. During initial tensile loading, MoS_2 nanosheets act as interlayer lubricants, mitigating stress concentrations and promoting uniform deformation of the MWCNT network via planar sliding. This lubrication effect delays structural failure, enhances strain tolerance, and improves wear resistance. Simultaneously, MoS_2 facilitates controlled microcrack formation, preventing catastrophic fracture while enhancing gauge sensitivity through predictable resistance variations [23,27]. As tensile strain increases, the MWCNT network absorbs additional mechanical energy through structural reconfiguration, complementing MoS_2's lubrication effect in the early deformation stages. However, once microcrack formation saturates, the gauge factor stabilizes, leading to a reduction in sensitivity.

This synergistic reinforcement mechanism, as demonstrated in Fig. 5 **(a)**, offers a scalable, environmentally friendly, and cost-effective approach for developing robust, high-performance wearable electronics, implantable biomedical devices, and soft robotics, where mechanical durability and sensing accuracy are critical. Meanwhile, exploring how the lubrication-enhanced strain sensing mechanism translates to state-of-the-art micro-cylindrical architectures could extend its application to fiber-based electronics, smart textiles, and flexible surgical robotics, where strain-adaptive and integrable sensing solutions are highly sought after [48]. Additionally, phase engineering of MoS_2 and other transition metal dichalcogenides (TMDs) remains an important avenue for optimizing both sensing performance and mechanical properties. Investigating the distinct electromechanical and tribological behaviors of pure 1 T or hybrid 1 T/2H phases could provide deeper insights into enhancing gauge sensitivity and structural resilience [49].

3.4. Application in physiological signal detection

As shown in Fig. 5**(b)**, the sensor effectively captured the characteristic waveform of blinking, displaying sharp peaks corresponding to the contraction and relaxation phases of the orbicularis oculi muscle, and it clearly reflects a slightly longer relaxation duration compared to contraction action [50]. For the frontalis muscle during voluntary frowning, larger amplitude peaks in the relative resistance change indicated stronger muscle contractions. Superimposed oscillations at the peak regions suggested fluctuations in muscle fiber recruitment during sustained contraction [51]. The sensor also recorded consistent peaks and valleys for wrist flexor activity during wrist flexion, with negative $\Delta R/R_0$ values in the extension phase reflecting the wrist's over-neutral position and passive contraction, resulting in reduced resistance. Additionally, the sensor monitored the extensor carpi radialis longus during the fist clenching and the tibialis anterior during ankle dorsiflexion, capturing complex stabilizer muscle interactions and varying phasic forces. Both motions exhibited secondary peaks superimposed on primary peaks, indicating co-activation of synergistic muscles [14,52]. Furthermore, the consistent return of $\Delta R/R_0$ to a stable baseline across all motions demonstrated the sensor's effective calibration, stability, and resistance to noise or artifact interference.

For swallowing and non-swallowing event classification, as detailed in **Section 2.5** and shown in Fig. 5**(c)**, the baseline performance of the default InceptionTime model, configured with kernel sizes of (10, 20, 40) and six inception blocks, achieved an initial accuracy of 0.580. This was attributed to the default kernel sizes corresponding to temporal windows of 0.02–0.08 s at a 500 Hz sampling rate. While sufficient for capturing fine-grained local patterns, this configuration was inadequate for modeling the longer temporal dependencies required to effectively differentiate swallowing events. To address this limitation, we systematically increased the kernel size, leading to a significant performance improvement. Optimal accuracy of 0.980 was achieved with an eight-fold increase in kernel size (80, 160, 320), beyond which further enlargement (up to 10 ×) yielded no additional gains, indicating saturation in performance improvements.

Given the dataset comprised only two-channel time-series data, we hypothesized that the default depth of six inception blocks might be excessive, potentially leading to overfitting. To evaluate this, we varied the number of inception blocks while maintaining the optimized kernel sizes. Reducing the depth to four inception blocks maintained the peak accuracy (0.980) while reducing model complexity. Increasing the number of blocks beyond six, up to 12, provided marginal accuracy gains, peaking at 0.990 with 10 blocks, but the added computational cost outweighed the minimal performance improvement. Thus, four inception blocks were selected as the optimal balance between accuracy and efficiency. Further evaluation focused on assessing the necessity of three kernel sizes. Experiments with reduced configurations, such as (80, 160), (80, 320), and (160, 320), resulted in accuracy drops to 0.820, 0.940, and 0.900, respectively, confirming that three kernel sizes (80, 160, 320) were necessary to maintain optimal classification performance.

The fine-tuned InceptionTime model demonstrated strong classification performance, as reflected in multiple evaluation metrics (Fig. 5 **(c)**). An overall F1-score of 0.98 and high AUC values for each class underscored the model's strong discriminatory power. Specifically, ROC curves (one-vs-rest) yielded AUCs of 0.97 for "Liquid" and "Coughing," 0.99 for "Semi Solid" and "Solid," and 1.00 for "Speaking 'O'," indicating high sensitivity and specificity with minimal class overlap. The confusion matrix further validated these results, showing high true positive counts across all classes and minimal misclassifications–one each in the "Liquid" and "Coughing" categories. These findings emphasize the model's robustness and reliability in distinguishing swallowing from non-swallowing events.

In terms of computational efficiency, InceptionTime maintains a relatively compact architecture with 7.02×10^6 parameters and a computational complexity of 5.61×10^{10} FLOPS. This lightweight structure contrasts with more complex deep learning models, such as Transformers, which require significantly higher computational resources due to the attention mechanism [53]. The efficiency of InceptionTime makes it well-suited for real-time processing on resource-constrained IoT devices, a critical requirement for continuous swallow monitoring in clinical and wearable applications. Additionally, its scalability allows for adaptation to varying and large time-series datasets without significant performance degradation. Despite the model's strong performance, the limited dataset size constrained its generalizability. Future work will focus on expanding the dataset to encompass a broader range of physiological variations and demographic groups. Further refinements will include advanced data augmentation techniques and domain adaptation strategies to enhance model robustness. Additionally, hybrid models integrating InceptionTime with other architectures, such as ConvTimeNet and ModernTCN [54], will be explored to leverage their ability to capture cross-variable dependencies and improve classification accuracy and reliability.

4. Conclusion

This study explored the exfoliation-based lubrication properties of 2H-MoS_2 and developed a MoS_2-enhanced piezoresistive sensor using MWCNT buckypaper. The lubrication effect of MoS_2 significantly modulated the microstructural evolution under small strain levels, leading to a 3881.5 % enhancement in gauge factor and improvements in fracture strain and toughness by 53.93 % and 89.17 %, respectively, compared to pure MWCNT systems. These enhancements effectively address the long-standing trade-off between sensitivity and strain tolerance, enabling precise and continuous monitoring of subtle biomotions while maintaining exceptional linearity, low hysteresis, and robust durability. The proposed MolyMWCNT-BP system represents a scalable and high-performance sensing solution for wearable and implantable health monitoring applications. Meanwhile, we integrated a fine-tuned InceptionTime model to enhance sensing capabilities, achieving a classification accuracy (F1-score) of 98 % for swallowing activities. This highlights the potential of AI-driven health monitoring systems leveraging piezoresistive sensors for real-time physiological motion detection.

CRediT authorship contribution statement

Ke-Yu Yao: Writing – original draft, Visualization, Validation, Investigation, Formal analysis, Data curation. **Derek Ka-Hei Lai:** Writing – original draft, Visualization, Software, Investigation, Formal analysis, Data curation. **Hyo-Jung Lim:** Investigation, Formal analysis, Data curation. **Bryan Pak-Hei So:** Writing – original draft, Investigation, Data curation. **Andy Chi-Ho Chan:** Validation, Software, Investigation. **Patrick Yiu-Man Yip:** Validation, Software, Investigation. **Duo Wai-Chi Wong:** Writing – review & editing, Supervision, Project administration, Funding acquisition. **Bingyang Dai:** Writing – review & editing, Validation, Methodology. **Xin Zhao:** Resources, Project administration, Conceptualization. **Siu Hong Dexter Wong:** Writing – review & editing, Supervision, Project administration, Methodology, Conceptualization. **James Chung-Wai Cheung:** Writing – review & editing, Supervision, Resources, Project administration, Methodology, Funding acquisition, Conceptualization.

Declaration of competing interest

The authors declare that they have no known competing financial interests or personal relationships that could have appeared to influence the work reported in this paper.

Acknowledgements

This study was supported by the Health and Medical Research Fund from the Health Bureau of Hong Kong (reference number: 21221871).

This study was approved by the Institutional Review Board of the Hong Kong Polytechnic University (ethical approval code: HSEARS20230302009). The authors would like to express their gratitude to the Industrial Centre of The Hong Kong Polytechnic University for their invaluable assistance with sample preparation and technical advice.

Appendix A. Supplementary data

Supplementary data to this article can be found online at https://doi.org/10.1016/j.matdes.2025.113861.

Data availability

Data will be made available on request.

References

[1] N.A. Ramli, A.N. Nordin, N.Z. Azlan, Review on strain sensors for detection of human facial expressions recognition systems, International Journal of Nanoelectronics & Materials 13 (3) (2020) 445–472.

[2] M.H.G. Monje, G. Foffani, J. Obeso, Á. Sánchez-Ferro, New sensor and wearable technologies to aid in the diagnosis and treatment monitoring of parkinson's disease, Annu. Rev. Biomed. Eng. 21 (1) (2019) 111–143.

[3] F.Q. Al-Khalidi, R. Saatchi, D. Burke, H. Elphick, S. Tan, Respiration rate monitoring methods: A review, Pediatr. Pulmonol. 46 (6) (2011) 523–529.

[4] O. Ortega, A. Martín, P. Clavé, Diagnosis and management of oropharyngeal dysphagia among older persons, State of the Art, J Am Med Dir Assoc 18 (7) (2017) 576–582.

[5] B.P. So, T.T. Chan, L. Liu, C.C. Yip, H.-J. Lim, W.-K. Lam, D.W. Wong, D.S. Cheung, J.C. Cheung, Swallow detection with acoustics and accelerometric-based wearable technology: a scoping review, Int. J. Environ. Res. Public Health (2023).

[6] O. Amft, G. Tröster, Recognition of dietary activity events using on-body sensors, Artif Intell Med 42 (2) (2008) 121–136.

[7] J.M. Fontana, P.L. Melo, E.S. Sazonov, Swallowing detection by sonic and subsonic frequencies: a comparison, Annu Int Conf IEEE Eng Med Biol Soc 2011 (2011) 6890–6893.

[8] M. Amjadi, K.U. Kyung, I. Park, M. Sitti, Stretchable, skin-mountable, and wearable strain sensors and their potential applications: a review, Adv. Funct. Mater. 26 (11) (2016) 1678–1698.

[9] Y.-F. Liu, Q. Liu, Y.-Q. Li, P. Huang, J.-Y. Yao, N. Hu, S.-Y. Fu, Spider-inspired ultrasensitive flexible vibration sensor for multifunctional sensing, ACS Appl. Mater. Interfaces 12 (27) (2020) 30871–30881.

[10] L. Li, H. Xiang, Y. Xiong, H. Zhao, Y. Bai, S. Wang, F. Sun, M. Hao, L. Liu, T. Li, Z. Peng, J. Xu, T. Zhang, Ultrastretchable fiber sensor with high sensitivity in whole workable range for wearable electronics and implantable medicine, Adv. Sci. 5 (9) (2018) 1800558.

[11] K. Ke, Z. Sang, I. Manas-Zloczower, Stretchable elastomer composites with segregated filler networks: effect of carbon nanofiller dimensionality, Nanoscale Adv. 1 (6) (2019) 2337–2347.

[12] M. Iqra, F. Anwar, R. Jan, M.A. Mohammad, A flexible piezoresistive strain sensor based on laser scribed graphene oxide on polydimethylsiloxane, Sci. Rep. 12 (1) (2022) 4882.

[13] R. Yang, H. Song, Z. Zhou, S. Yang, X. Tang, J. He, S. Liu, Z. Zeng, B.-R. Yang, X. Gui, Ultra-sensitive, multi-directional flexible strain sensors based on an MXene film with periodic wrinkles, ACS Appl. Mater. Interfaces 15 (6) (2023) 8345–8354.

[14] X. Pang, Q. Zhang, Y. Zhao, X. Liang, L. Wang, Y. Shao, Regulation of sulfur vacancies in vertical nanolamellar MoS2 for ultrathin flexible piezoresistive strain sensors, J. Mater. Sci. Technol. 141 (2023) 56–65.

[15] S.A. Bhakhar, M. Tannarana, P.M. Pataniya, N.F. Patel, B. Chauhan, G.K. Solanki, Flexible paper-based piezo-resistive sensor functionalized by MoS2 nanosheets, J. Mater. Sci. Mater. Electron. 34 (11) (2023) 994.

[16] S.-C. Her, W.-C. Hsu, Strain and temperature sensitivities along with mechanical properties of CNT buckypaper sensors, Sensors (2020).

[17] D. Singh, A. Rawal, Tensile mechanics of buckypaper: Bridging the disconnect between disordered structure and carbon nanotube properties, Carbon 190 (2022) 299–311.

[18] M.S. Sokolikova, C. Mattevi, Direct synthesis of metastable phases of 2D transition metal dichalcogenides, Chem. Soc. Rev. 49 (12) (2020) 3952–3980.

[19] A. Chhetry, M. Sharifuzzaman, H. Yoon, S. Sharma, X. Xuan, J.Y. Park, MoS2-decorated laser-induced graphene for a highly sensitive, hysteresis-free, and reliable piezoresistive strain sensor, ACS Appl. Mater. Interfaces 11 (25) (2019) 22531–22542.

[20] M. Dong, E. Bilotti, H. Zhang, C.S. Boland, D.G. Papageorgiou, High performing piezoresistive MoS2/epoxy strain sensors for structural health monitoring, Polymer 309 (2024) 127449.

[21] H. Park, J. Park, S.-W. Kang, S.-H. Jeong, Nanoarchstructured MoS2-based strain sensor with exceptional gauge factor, Sens. Actuators, A 380 (2024) 116050.

[22] Q. Ji, Z. Jing, J. Shen, Y. Hu, L. Chang, L. Lu, M. Liu, J. Liu, Y. Wu, Dual-responsive soft actuators with integrated sensing function based on 1T-MoS2 composite, Adv. Intell. Syst. 3 (7) (2021) 2000240.

[23] D. Qiu, Y. Chu, H. Zeng, H. Xu, G. Dan, Stretchable MoS2 electromechanical sensors with ultrahigh sensitivity and large detection range for skin-on monitoring, ACS Appl. Mater. Interfaces 11 (40) (2019) 37035–37042.

[24] F. Wang, D. Su, K. Ma, B. Qin, B. Li, J. Li, C. Zhang, Y. Xin, Z. Huang, W. Yang, S. Wang, X. He, Reliable and scalable piezoresistive sensors with an MXene/MoS2 hierarchical nanostructure for health signals monitoring, ACS Appl. Mater. Interfaces 15 (37) (2023) 44001–44011.

[25] H. Wang, J. Liu, H. Cui, Y. Liu, J. Zhu, H. Wang, G. Song, Z. Li, D. Chen, Strain sensor with high sensitivity and large response range based on self-assembled

elastic-sliding conductive networks, ACS Appl. Electron. Mater. 3 (4) (2021) 1758–1770.
[26] H. Li, J. Wang, S. Gao, Q. Chen, L. Peng, K. Liu, X. Wei, Superlubricity between MoS2 monolayers, Adv. Mater. 29 (27) (2017) 1701474.
[27] J. Wang, W. Ming, L. Chen, T. Song, M. Yele, H. Zhang, L. Yang, G. Sarula, B. Liang, L. Yan, G. Wang, MoS2 Lubricate-toughened MXene/ANF composites for multifunctional electromagnetic interference shielding, Nano-Micro Letters 17 (1) (2024) 36.
[28] S. Wan, Y. Li, J. Peng, H. Hu, Q. Cheng, L. Jiang, Synergistic toughening of graphene oxide–molybdenum disulfide–thermoplastic polyurethane ternary artificial nacre, ACS Nano 9 (1) (2015) 708–714.
[29] M.N. Alam, V. Kumar, D.-J. Lee, J. Choi, Synergistically toughened silicone rubber nanocomposites using carbon nanotubes and molybdenum disulfide for stretchable strain sensors, Compos. B Eng. 259 (2023) 110759.
[30] M.A. Morid, O.R.L. Sheng, J. Dunbar, Time series prediction using deep learning methods in healthcare, ACM Trans. Manage. Inf. Syst. 14 (1) (2023). Article 2.
[31] K. Liao, W. Wang, A. Elibol, L. Meng, X. Zhao, N.Y. Chong, Does deep learning REALLY outperform non-deep machine learning for clinical prediction on physiological time series? ArXiv abs/2211.06034 (2022).
[32] Y. Hua, Z. Zhao, R. Li, X. Chen, Z. Liu, H. Zhang, Deep learning with long short-term memory for time series prediction, IEEE Commun. Mag. 57 (6) (2019) 114–119.
[33] T. Lin, Y. Wang, X. Liu, X. Qiu, A survey of transformers, AI Open 3 (2022) 111–132.
[34] J. Ding, X. Li, X. Kang, V.N. Gudivada, A case study of the augmentation and evaluation of training data for deep learning, J. Data and Information Quality 11 (4) (2019). Article 20.
[35] L. Rasmy, Y. Xiang, Z. Xie, C. Tao, D. Zhi, Med-BERT: pretrained contextualized embeddings on large-scale structured electronic health records for disease prediction, NPJ Digit Med 4 (1) (2021) 86.
[36] H. Ismail Fawaz, B. Lucas, G. Forestier, C. Pelletier, D.F. Schmidt, J. Weber, G.I. Webb, L. Idoumghar, P.-A. Muller, F. Petitjean, InceptionTime: Finding AlexNet for Time Series Classification, 2019, p. arXiv:1909.04939.
[37] W. Dong, K. Sheng, B. Huang, K. Xiong, K. Liu, X. Cheng, Stretchable self-powered TENG sensor array for human-robot interaction based on conductive ionic gels and LSTM neural network, IEEE Sens. J. 24 (22) (2024) 37962–37969.
[38] A. Greco, G. Valenza, A. Lanata, E.P. Scilingo, L. Citi, cvxEDA: a convex optimization approach to electrodermal activity processing, IEEE Trans. Biomed. Eng. 63 (4) (2016) 797–804.
[39] X. Wang, X. Hu, Z. Qu, T. Sun, L. Huang, S. Xu, MoS2@MWCNTs with rich vacancy defects for effective piezocatalytic degradation of norfloxacin via innergenerated-H2O2: enhanced nonradical pathway and synergistic mechanism with radical pathway, ACS Appl. Mater. Interfaces 16 (20) (2024) 26257–26271.
[40] V.M.T.M. Selvakumari, R. Marnadu, I.M. Ashraf, MoS2 blended MWCNT hybrid nanocomposites and its enhanced super capacitive features, Solid State Commun. 375 (2023) 115345.
[41] Y. Li, X. Lu, H. Wang, C. Xie, G. Yang, C. Niu, Growth of ultrafine SnO2 nanoparticles within multiwall carbon nanotube networks: non-solution synthesis and excellent electrochemical properties as anodes for lithium ion batteries, Electrochim. Acta 178 (2015) 778–785.
[42] C. Archana, S. Harish, R. Abinaya, J. Archana, M. Navaneethan, Interface modified MoS2/CNT with enhanced power factor via energy filtering effect for flexible thermoelectric applications, Sens. Actuators, A 348 (2022) 113938.
[43] C. Zhang, Z. Wang, S. Bhoyate, T. Morey, B. Neria, V. Vasiraju, G. Gupta, S. Palchoudhury, P. Kahol, S. Mishra, F. Perez, R. Gupta, MoS2 decorated carbon nanofibers as efficient and durable electrocatalyst for hydrogen evolution reaction, C 3 (2017) 33.
[44] W. Yan, H.-R. Fuh, Y. Lv, K.-Q. Chen, T.-Y. Tsai, Y.-R. Wu, T.-H. Shieh, K.-M. Hung, J. Li, D. Zhang, C.Ó. Coileáin, S.K. Arora, Z. Wang, Z. Jiang, C.-R. Chang, H.-C. Wu, Giant gauge factor of Van der Waals material based strain sensors, Nat. Commun. 12 (1) (2021) 2018.
[45] J. He, J. Feng, B. Huang, W. Duan, Z. Chen, J. Huang, B. Li, Z. Zhou, Z. Zeng, X. Gui, Multi-directional strain sensor based on carbon nanotube array for human motion monitoring and gesture recognition, Carbon 226 (2024) 119201.
[46] S.J. Paul, I. Elizabeth, S. Srivastava, J.S. Tawale, P. Chandra, H.C. Barshilia, B. K. Gupta, Epidermal inspired flexible sensor with buckypaper/PDMS interfaces for multimodal and human motion monitoring applications, ACS Omega 7 (42) (2022) 37674–37682.
[47] H. Dong, J. Sun, X. Liu, X. Jiang, S. Lu, Highly sensitive and stretchable MXene/CNTs/TPU composite strain sensor with bilayer conductive structure for human motion detection, ACS Appl. Mater. Interfaces 14 (13) (2022) 15504–15516.
[48] W. Hongyang, W. Hao, Y. Dong, Z. Chenyang, W. Qingshuang, W. Sen, Z. Zhiwei, Z. Mingtao, W. Hanghang, H. YongAn, Micro-cylindrical/fibric electronic devices: materials, fabrication, health and environmental monitoring, Soft Science 4 (4) (2024) 41.
[49] S.S. Chou, Y.-K. Huang, J. Kim, B. Kaehr, B.M. Foley, P. Lu, C. Dykstra, P. E. Hopkins, C.J. Brinker, J. Huang, Controlling the metal to semiconductor transition of MoS2 and WS2 in solution, J. Am. Chem. Soc. 137 (5) (2015) 1742–1745.
[50] M. Sekulic-Jablanovic, N.D. Ullrich, D. Goldblum, A. Palmowski-Wolfe, F. Zorzato, S. Treves, Functional characterization of orbicularis oculi and extraocular muscles, J. Gen. Physiol. 147 (5) (2016) 395–406.
[51] O. Guntinas-Lichius, G.F. Volk, K.D. Olsen, A.A. Mäkitie, C.E. Silver, M.E. Zafereo, A. Rinaldo, G.W. Randolph, R. Simo, A.R. Shaha, V. Vander Poorten, A. Ferlito, Facial nerve electrodiagnostics for patients with facial palsy: a clinical practice guideline, Eur. Arch. Otorhinolaryngol. 277 (7) (2020) 1855–1874.
[52] N. van Elk, M. Faes, H. Degens, J.G. Kooloos, J.A. de Lint, M.T. Hopman, The application of an external wrist extension force reduces electromyographic activity of wrist extensor muscles during gripping, J Orthop Sports Phys Ther 34 (5) (2004) 228–234.
[53] K. Han, Y. Wang, H. Chen, X. Chen, J. Guo, Z. Liu, Y. Tang, A. Xiao, C. Xu, Y. Xu, Z. Yang, Y. Zhang, D. Tao, A survey on vision transformer, IEEE Trans Pattern Anal Mach Intell 45 (1) (2023) 87–110.
[54] M. Cheng, J. Yang, T. Pan, Q. Liu, Z. Li, ConvTimeNet: A deep hierarchical fully convolutional model for multivariate time series analysis, ArXiv abs/2403.01493 (2024).